Letter Vol. 50, No. 21/1 November 2025/Optics Letters 6582

Optics Letters

On-chip wide-FSR silicon optical filter with high extinction ratio and compact footprint

Sourabh Jain,[1,*] Ray T. Chen,[2,3] and Mukesh Kumar[4]

[1]Department of Electronics and Communication Engineering, Indian Institute of Information Technology, Bhopal, India
[2]Department of Electrical and Computer Engineering, University of Texas at Austin, Austin, Texas 78758, USA
[3]Omega Optics Inc., 8500 Shoal Creek Blvd., Bldg. 4, Suite 200, Austin, Texas 78757, USA
[4]Department of Electrical Engineering, Indian Institute of Technology, Indore 453552, India
*sourabh.jain@iiitbhopal.ac.in

Received 4 September 2025; revised 27 September 2025; accepted 29 September 2025; posted 3 October 2025; published 22 October 2025

Optical filters play a crucial role in advanced optical computing, communication, and sensing applications, and those featuring an ultra-large free spectral range (FSR) are particularly significant. These filters offer access to numerous finely tuned wavelength channels, significantly enhancing the optical transmission capacity and performance of sensing applications. However, the existing wide-FSR filter designs are hampered by limitations in cavity length, fabrication complexity, or the need for additional active-tuning controls. To address these challenges, we present what we believe to be a novel tapered-cavity-coupled asymmetric-gratings that leverages an inter-mode coupling phenomenon, enabling wide-FSR operation with nanometer-scale full width at half maximum (FWHM) in a compact on-chip silicon device. Our approach experimentally demonstrates a single resonant peak of 1.2 nm FWHM and 14 dB extinction ratio, alongside a theoretically predicted FSR exceeding 200 nm, all within a highly miniaturized footprint of 18 μm^2. This compact and fabrication-tolerant architecture offers a scalable route for implementing high-performance single-channel filters across a broad spectral range, making it highly relevant for next-generation optical communication, quantum photonics, and lab-on-chip sensing platforms.

https://doi.org/10.1364/OL.578238

Integrated photonics has emerged as a cornerstone of modern optical technologies, enabling the miniaturization and enhancement of optical systems on chip-scale platforms [1]. These systems are pivotal for a wide range of applications, including optical communication [2], quantum computing [3], and optical sensing [4]. At the heart of many integrated photonic circuits lies the need for optical filters, which perform critical functions such as wavelength selection, noise suppression, and signal isolation [5]. The demand for on-chip filters is particularly pronounced in advanced technologies like wavelength-division multiplexing (WDM) for dense optical networks [6], quantum light sources for scalable quantum photonics [7], and high-resolution optical sensors and spectroscopy techniques where precise spectral discrimination is crucial for accurate detection of target analytes [8].

Many techniques have been explored to realize wavelength-selective filtering of broadband optical signals, yet most inherently produce multiple transmission peaks or broad passbands. For example, microring resonators produce a periodic comb of resonances across the spectrum, leading to side modes that make isolating a single-channel challenging [9]. Arrayed waveguide gratings (AWGs) similarly output many fixed channels simultaneously [10], and Mach–Zehnder interferometers create periodic fringes [11]. Despite significant progress, aforementioned conventional on-chip filters often fall short of meeting the stringent requirements of modern applications, where high-quality individual channels must exhibit high side-mode suppression ratios along with high isolation bandwidths and precisely controlled channel spacing to minimize crosstalk in dense WDM systems. For instance, MRR-based filters, while offering compact designs and high-quality factors (Q), are constrained by narrow FSRs and susceptibility to temperature variations. On the other hand, MZI-based filters provide broader bandwidths and athermal performance, but require large footprints, limiting their use in densely packed photonic circuits. Periodic metastructures such as Bragg-gratings-based optical filters, can be designed for arbitrary but controllable spectral profiles [12]. However, conventional single-mode optical Bragg waveguides often exhibit periodic filtering profiles, necessitating complex cascading or additional off-chip filtering for applications requiring narrowband or flat spectral isolation. Techniques such as mode splitting in whispering-gallery modes have reduced temperature sensitivity but still fail to address FSR limitations comprehensively [13].

To address these challenges, a single transmission peak (i.e., an FSR-free single-channel filter) is highly desirable to isolate one wavelength with high spectral resolution [14–16]. Recently, Tang *et al.* proposed a multiplexed array of FSR-free nanobeam cavities using asymmetric Bragg mirrors to suppress higher-order modes, yielding a single narrow peak over >350 nm. However, fabrication sensitivity (hole size, pitch, and asymmetry) could limit scalability and yield in such complex structure. Although such a narrowband filter improves channel selectivity in

dense WDM communications, enables precise line selection in on-chip spectroscopy, and enhances sensor resolution by focusing on one resonance. Equally important, if each filter has only one passband in the telecom range, multiple devices can be combined to scale up to a multi-channel system without crosstalk. In fact, using an array of single-peak filters, one can cover many wavelengths independently, significantly increasing the number of usable channels [17].

To achieve this, multimode photonics is playing a vital role, particularly through the exploitation of inter-mode interference in multimode waveguides, enables the realization of single, isolated transmission peaks with large effective FSRs, enhanced spectral selectivity, and compact footprints, effectively overcoming footprint limitations of single-mode filter architectures. Within this framework, asymmetric gratings based on multimode optical filters have emerged as promising candidates, offering arbitrary yet controllable optical characteristics, and numerous techniques have been developed to harness their potential [18,19]. For instance, Astudillo *et al*., demonstrated, an antisymmetric 1D photonic crystal in a Si multimode waveguide was used to realize a 200 nm-wide stopband with Fabry–Perot-like localized modes inside it [20]. However, achieving asymmetry in such nano-scale structures is extremely fabrication sensitive. In another effort, Jiang *et al*., designed and demonstrated asymmetric Y-junction to effectively suppress Bragg reflections and enhance mode-selective filtering in multimode waveguides [21]. Recently, Chen *et al*. reported an on-chip mode converter and filter based on asymmetrical directional couplers attributing >29 dB mode extinction ratio, and broad 80 nm bandwidth within a footprint of only 20.8 μm^2 [22]. Beyond these approaches, an additional avenue in multimode optical propagation involves the control of dispersion behavior. For example, Torrijos *et al.* demonstrated slow-light bimodal interferometric behavior in an integrated one-dimensional asymmetric photonic crystal waveguide and successfully applied it for ethanol detection [23].

Previously, we demonstrated a novel approach to achieving a narrow transmission peak with large FSR attributes in a dual-perturbed Bragg grating structure, where both sets of gratings were separated by a cavity section. The proposed device was fabricated on a highly compact area and exhibited high suppression ratio of 20 dB of the near-resonant peak of the side lobes [24]. Such dual sets of gratings are required to align the individual modes (fundamental and higher order) so that they constructively interfere, allowing a narrow spectral band at the output. Recently, we have also reported the theoretical framework of dispersion characteristics of the resonant mode in such structure [25]. However, the fabrication of the reported device is complex because of the presence of two different grating periods simultaneously. To relax fabrication complexity while maintaining precise control over individual modes, we propose two sets of asymmetric grating structures connected by a tapered-cavity section, which enables the required spectral tuning while preserving the intended optical performance. Instead of employing two different gratings, width variations are used to achieve the desired mode manipulation. This approach relaxes fabrication sensitivity issues, as width optimization is generally easier to reproduce lithographically than grating period optimization.

The fabricated device exhibits a narrow transmission peak of 1.2 nm FWHM with a high extinction ratio of 14 dB. The numerically predicted value of the FSR is greater than 200 nm,

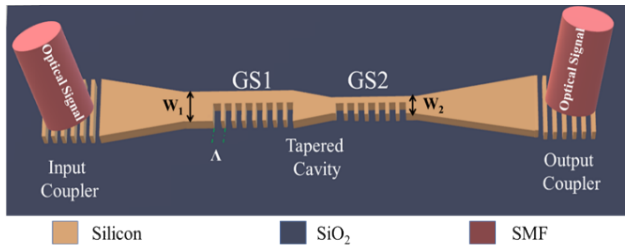

Fig. 1. Schematic view of the tapered cavity coupled asymmetric grating-based device in silicon on insulator (SOI) platform with input and output grating couplers. The two sets of gratings, grating set one (GS1) and grating set 2 (GS2), are coupled with a 2 µm-long tapered-cavity section. The optimized grating parameters for both GS1 and GS2 are Λ = 385 nm and the duty cycle = 60%. The widths of GS1 and GS2 are W1 = 850 nm and W2 = 650 nm, respectively. The optical signal was fed/collected through a single-mode fiber, as shown in red.

which makes the device ideal for dense WDM systems, precision spectroscopy, and ultra-sensitive optical sensing, and opens opportunities for scalable multi-channel photonic integration without performance degradation. Figure 1 presents a schematic of the proposed multimode optical filter, which integrates two Bragg grating sections, for example, grating set 1 and 2 (GS1 and GS2) connected by a linearly tapered cavity. The device also incorporates optimized input and output grating couplers designed to efficiently couple TE-polarized light between an optical fiber and the on-chip waveguide, thereby simplifying the measurement process. Both Bragg grating sections consist of sidewalls at one of the edges, which induce asymmetry in the structure. This is essential because it ensures the excitation of the first-order mode; otherwise, only the fundamental mode and even order modes would be sustained, resulting in the absence of the desired inter-mode coupling and, consequently, no formation of the targeted single narrow transmission peak. To obtain relax the fabrication complexity, GS1 and GS2 are designed with the same period and duty cycle, while their widths are optimized in such a way that the relative spectral shift arising from both the GS1 and GS2 the distinct effective refractive indices (ERIs) of the optical modes. A small, tapered-cavity section is introduced between these sets of gratings offer distinctive advantages in two ways: (i) it improves the coupling of the optical signal between two grating sets by avoiding sudden mode mismatch due to distinct width and (ii) its optimized length allows phase matching of the optical signal at the second set of the grating so that a single transmission peak can be realized in the output spectrum. The proposed device was partially etched horizontally with an etch depth of 150 nm, whereas the corrugation widths of GS1 and GS2 were 850 nm and 650 nm, respectively.

To determine the optimal input waveguide width capable of supporting at least two well-confined guided modes, a detailed modal analysis was performed by systematically varying the silicon waveguide width, as illustrated in Fig. 2(a). The results show that the first-order transverse mode emerges once the waveguide width exceeds approximately 600 nm. The effective refractive index of the fundamental mode is denoted as n^0_{eff}, that of the first-order mode as n^1_{eff}, and that of the second-order mode as n^2_{eff}. Among these, n^0_{eff} is the highest, owing to the strong confinement of the fundamental mode within the high-index

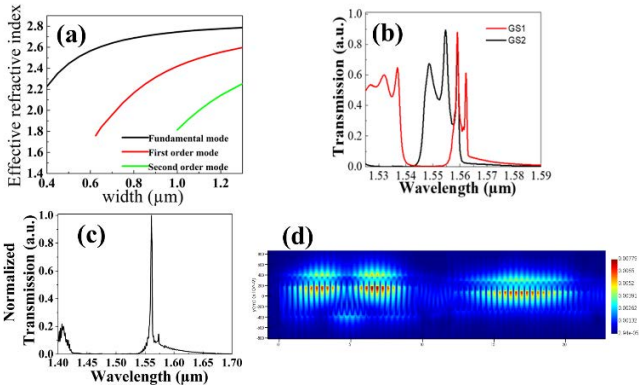

Fig. 2. (a) Effective refractive indices of optical modes (TE only) as a function of the waveguide width at $\lambda = 1550$ nm. (b) Optical transmission for individual sets of gratings as a function of wavelength. 2.5D FDTD is used to calculate the optical response, which provides a better approximation of the result with less memory and fast calculation. (c) Simulated optical transmission characteristics of full-length devices using the 3D FDTD method. A single transmission peak was observed for a wide range of wavelengths, with an FSR exceeding 200 nm. (d) Electric field distribution of the propagating mode at $\lambda = 1.558$ μm.

silicon core. In contrast, higher-order modes (n^1_{eff} and n^2_{eff}) exhibit reduced confinement, with a greater fraction of the optical field extending into the low-index cladding, thereby lowering their effective indices. This disparity in modal confinement results in distinct phase constants ($\beta = \frac{2\pi n_{eff}}{\lambda}$), which correspond to different phase velocities and enable mutual coupling between the co-propagating and counter-propagating components of these modes. By tuning the relative phase relationship between the fundamental and first-order modes, the filter response can be engineered to produce a single, isolated passband in the transmission spectrum. Furthermore, to achieve a narrow FWHM with high sidelobe suppression ratio, a secondary grating section with a slightly reduced waveguide width is incorporated, introducing a controlled spectral offset between the two grating responses and thereby enhancing overall filter selectivity.

Figure 2 presents the simulated optical response of the proposed structure, obtained through numerical modeling in the Lumerical Solutions design environment. For clarity, Fig. 2(b) depicts the spectral characteristics of each grating section when analyzed independently. When these two sections are connected via the tapered cavity, the Bragg reflections generated by the fundamental and first-order modes interact in a manner that satisfies the phase-matching requirement at a specific wavelength. This constructive interaction enhances the desired transmission channel, while out-of-band components are strongly attenuated. The corresponding normalized transmission spectrum of the proposed device, showing a single transmission peak with a free spectral range exceeding 200 nm, and the electric field distribution at the resonant peak wavelength are shown in Figs. 2(c) and 2(d), respectively. A slight elevation on the higher-wavelength side of the main resonance is visible, which originates from residual overlap between the individual passbands of the two gratings. This artifact can be reduced by refining parameters such as grating, duty cycle, and corrugation depth cavity length to achieve improved spectral isolation.

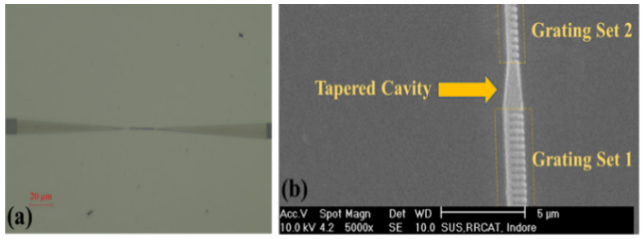

Fig. 3. (a) Microscopic view of full-length device with connected grating coupler. (b) Scanning electron microscopic view of the center of the fabricated device.

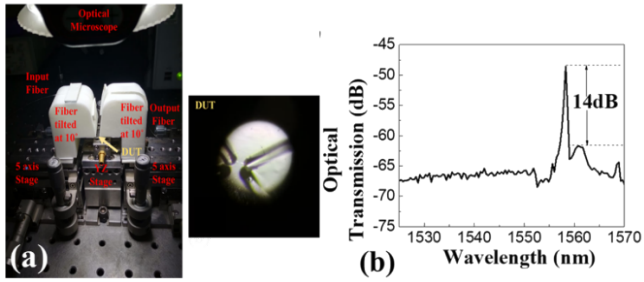

Fig. 4. (a) Photograph of the measurement setup. The device is mounted on alignment stages. The optical signal is fed to the device at an angle of 100 with respect to the vertical axis through a grating coupler. The inset shows the microscopic view of the device and optical fibers aligned across the device. (b) Measured optical transmission characteristic of the fabricated device in a wavelength range of 1.53 μm < λ < 1.57 μm; the transmission peak observed at $\lambda = 1558.3$ nm.

Fabrication began with piranha cleaning, followed by two-step HSQ spin coating (500 rpm for 10 s, then 4500 rpm for 45 s) to obtain an ~80 nm film, and a 2 min prebake at 180°C for surface uniformity. Coated samples were patterned via electron beam lithography (10 μm aperture, 10 kV, 23 pA, 360 μC/cm^2), developed for 4 min, and etched by RIE using SF_6:CHF_3 (6:20 sccm), 15 mTorr, 30 W RF, and 1000 W plasma power. After pattern transfer, the hard mask was removed by immersing the samples in a 3% HF solution diluted in deionized water until the silicon surface was fully exposed. Finally, a 2 μm-thick SiO_2 passivation layer was deposited over the entire device to provide environmental protection. Optical microscope and SEM images of the fabricated structures are presented in Figs. 3(a) and 3(b), respectively.

Figure 4(a) shows a photograph of the experimental measurement setup, with the inset providing a top view of the device precisely aligned to the grating coupler. Figure 4(b) presents the experimentally measured optical response of the fabricated device. A well-defined single transmission peak was observed at $\lambda = 1558.3$ nm, exhibiting a high extinction ratio of 14 dB and a FWHM of 1.2 nm, corresponding to a quality factor (Q-factor) of approximately 1299. The measured spectrum also reveals high FSR characteristics within the accessible wavelength window of 1.53 μm < λ < 1.57 μm, limited by the range of the available tunable laser source. This result is in a well agreement with the simulated response shown in Fig. 2(c). It should be noted that a broadband light source, such as a supercontinuum laser, can also be employed to measure a wider spectral range. The overall insertion loss in the spectrum arises from

Table 1. Comparison of On-Chip Silicon Photonic Filters with Wide or FSR-Free Operation

Structure Type	FSR	Quality Factor	Extinction Ratio	Footprint	Platform	References
MRR/SM	5 nm	10,000	9 dB	14,400 μm^2	Si_3N_4/SiO_2 with GST	[26]
1D photonic crystal nanobeam/MM	>350 nm	2900	14.5 dB	215 × 120 μm²	SOI	[15]
Grating-assisted contra-directional coupler	>100 nm	700–800	20 dB	2×10^4 μm^2	SOI	[14]
Long-period grating couplers	-	390	10–15 dB	0.75 mm²	SOI	[19]
TW-like Fabry–Pérot resonator/MM	>200 nm	6821	19.8	6.6×10^3 μm²	SOI	[27]
Antisymmetric Bragg Gratings/MM	>200 nm	1298	14 dB	18 μm²	SOI	This work

multiple sources, including polarization-controller loss, grating-coupler inefficiency, free-space propagation loss, fiber-to-chip alignment errors, intrinsic device loss, and scattering at the fiber facets due to surface roughness. The measured results are in close agreement with numerical simulations, though a slight resonance wavelength shift is evident. This deviation is likely caused by differences between the simulated and actual refractive indices of the materials, or by minor fabrication inaccuracies such as deviations in grating period or duty cycle.

Table 1 represents a comparison of proposed device with some experimentally reported on-chip Si photonic filters designed for wide or FSR-free operation. While microring and photonic crystal nanobeam filters provide high Q-factors, they are constrained by either limited FSR or large device footprints. The proposed work unveils a pioneering multimode optical filter, leveraging tapered-cavity-coupled asymmetric gratings to achieve a single, sharp transmission peak of 1.2 nm FWHM and 14 dB extinction ratio within an exceptionally compact footprint of 18 μm^2. With a simulated FSR exceeding 200 nm and a measured Q-factor of approximately 1299, the device offers unmatched spectral precision and scalability, addressing longstanding challenges in dense WDM systems, precision spectroscopy, and high-sensitivity sensing. Its fabrication-tolerant design, enabled by width-optimized gratings and a streamlined tapered cavity, minimizes complexity while maximizing performance, paving the way for robust, high-yield photonic integration. This advancement not only enhances the efficiency of next-generation optical networks and quantum photonics but also sets a foundation for compact, versatile lab-on-chip platforms, heralding a new era of photonic innovation.

Acknowledgment. Authors would like to acknowledge the fabrication facilities provided by RRCAT Indore. Special thanks are extended to Dr. Arvind Kumar Srivastava and Dr. Pragya Tiwari for their valuable assistance in this work.

Disclosures. The authors declare no conflicts of interest.

Data availability. No data were generated or analyzed in the presented research.

REFERENCES

1. Z. Zhang, S. Zhang, X. Liu, *et al.*, Laser Photon. Rev. **19**, 2400155 (2025).
2. S. Jain, S. Rajput, V. Kaushik, *et al.*, Opt. Commun. **434**, 49 (2019).
3. S. Ning, H. Zhu, C. Feng, *et al.*, J. Lightwave Technol. **42**, 8189600 (2024).
4. S. Jain, M. H. Hlaing, K.-C. Fan, *et al.*, Appl. Phys. Rev. **12**, 011337 (2025).
5. D. Liu, H. Xu, Y. Tan, *et al.*, Microwave Opt. Technol. Lett. **63**, 2252 (2021).
6. N. Qi, Q. Ma, A. Li, *et al.*, IEEE J. Solid-State Circuits **60**, 3613 (2025).
7. L. Caspani, C. Xiong, B. J. Eggleton, *et al.*, Light: Sci. Appl. **6**, e17100 (2017).
8. W.-C. Lai, S. Chakravarty, X. Wang, *et al.*, Opt. Lett. **36**, 984 (2011).
9. P. Zheng, X. Xu, G. Hu, *et al.*, J. Lightwave Technol. **39**, 1429 (2021).
10. J. Zou, F. Sun, C. Wang, *et al.*, Opt. Laser Technol. **147**, 107656 (2022).
11. T. Yang, S. Zhang, T. Zhang, *et al.*, Opt. Exp. **33**, 639 (2025).
12. X. Wang, *Silicon Photonic Waveguide Bragg Gratings* (University of British Columbia, 2013).
13. X. Jiang, A. J. Qavi, S. H. Huang, *et al.*, Matter **3**, 371 (2020).
14. Z. Jin, Q. Ren, D. Liu, *et al.*, Opt. Lett. **49**, 6385 (2024).
15. R. Tang, C. Sun, K. Bao, *et al.*, Laser Photon. Rev. **18**, 2300828 (2024).
16. S. Yuan, L. Chen, Z. Wang, *et al.*, Nat. Commun. **12**, 5570 (2021).
17. C. Sun, Y. Yin, Z. Chen, *et al.*, PhotoniX **3**, 12 (2022).
18. L. G. Wright, W. H. Renninger, D. N. Christodoulides, *et al.*, Optica **9**, 824 (2022).
19. J. Høvik, M. Yadav, J. Wook Noh, *et al.*, Opt. Exp. **28**, 23936 (2020).
20. M. Mendez-Astudillo, H. Okayama, and H. Nakajima, Opt. Exp. **26**, 1841 (2018).
21. H. Qiu, J. Jiang, P. Yu, *et al.*, Opt. Lett. **41**, 2450 (2016).
22. X. Chen, X. Shi, P. Qiu, *et al.*, Opt. Lett. **47**, 4600 (2022).
23. L. Torrijos-Morán, A. Griol, and J. García-Rupérez, Light: Sci. Appl. **10**, 16 (2021).
24. S. Jain, S. Srivastava, S. Rajput, *et al.*, IEEE Sens. J. **20**, 3529 (2020).
25. S. Jain, N. Kumar, M. Kumar, *et al.*, in *Conference on Lasers and Electro-Optics/Pacific Rim* (Optica Publishing Group, 2024), p. P3_057.
26. J. Feldmann, N. Youngblood, C. D. Wright, *et al.*, Nature **569**, 208 (2019).
27. Y. Chen, Y. Zhao, Y. Shi, *et al.*, J. Lightwave Technol. **43**, 9258 (2025).